

# Romanechite, an Asymmetric Tunnel-Type $\text{MnO}_2$ , for Rechargeable Magnesium Battery Cathodes

Takashi Yabu, Reona Iimura, Akira Nasu, Toshihiko Mandai, Masaki Matsui, and Hiroaki Kobayashi\*

Rechargeable magnesium batteries are expected to serve as alternatives to lithium-ion batteries due to their advantages in high volumetric energy density, low cost, and safety, associated with using the magnesium metal anode. Tunnel-type manganese dioxides have been intensively explored as cathode materials due to their robust host structure and high operating potential. However, Hollandite ( $\alpha\text{-MnO}_2$ ), a standard tunnel-type  $\text{MnO}_2$  having  $2 \times 2$  channels, shows an irreversible structure change during magnesium intercalation, from a symmetric tunnel structure to an

asymmetric tunnel structure, due to the deviated Mg site from the tunnel center. Herein, an asymmetric  $3 \times 2$  tunnel-type  $\text{MnO}_2$ , Romanechite, is synthesized using a room-temperature alcohol solution process. The obtained Romanechite has plate-like nanoparticles and exhibits a discharge capacity of  $130 \text{ mAh g}^{-1}$  with no significant structure change during the discharge and recharge, demonstrating superior electrochemical magnesium intercalation/extraction efficiency and capacity retention at room-temperature operation.

## 1. Introduction

As the demand for lithium-ion batteries (LIBs) rises with the increasing prevalence of portable devices and electric vehicles, rechargeable magnesium batteries (RMBs) are emerging as a noteworthy alternative to alleviate this demand. RMBs are cost-effective compared to LIBs due to the abundance of magnesium in the Earth's crust. Furthermore, the magnesium metal anode has a potential for high volumetric capacity (higher than lithium metal) and safety (not forming dendrites) to enhance the battery life.<sup>[1]</sup>

One of the major challenges in the practical application of magnesium batteries is the strong Coulombic interaction between magnesium ions and anions in host structures at the cathodes; it brings low-rate capability and irreversible structure changes in the cathode active materials.<sup>[2]</sup> Although metal sulfide cathodes, such as Chevrel-type  $\text{Mo}_6\text{S}_8$ , reported by Aurbach et al., can exhibit high reversibility due to relatively weak interaction compared with metal oxides, they suffer from a low operating

voltage.<sup>[3]</sup> Hence, overcoming the slow magnesium-ion diffusion of oxide cathode materials is urgently required for high-voltage operation. Nanoparticulation is an effective solution to operate oxide cathode materials. For instance, in the spinel oxide  $\text{MgMn}_2\text{O}_4$  cathode, magnesium ions can only intercalate within 1 nm of the particle surface at room temperature; we reported that full magnesiation ( $270 \text{ mAh g}^{-1}$  discharge) is achieved using the ultrasmall  $\text{MgMn}_2\text{O}_4$  nanoparticles ( $\approx 2 \text{ nm}$ ).<sup>[4]</sup> Enhancing the specific surface area and shortening the ion pathway through nanoparticulation can achieve a high capacity close to the theoretical value, even at room temperature.

Manganese dioxides,  $\text{MnO}_2$ , have been investigated as a cathode material due to their high potential and capacity benefits.<sup>[5]</sup>  $\text{MnO}_2$  shows polymorphs; determining an ideal host structure against the magnesium ion insertion is important. During magnesium insertion, spinel-type  $\lambda\text{-MnO}_2$  undergoes a structural transformation to an electrochemically inactive rock-salt structure, whereas layered  $\delta\text{-MnO}_2$  strongly captures magnesium ions, inhibiting their extraction. Conversely, the tunnel structure, having a robust host framework with a 1D diffusion path, enables reversible intercalation/extraction of magnesium ions. The tunnel structure holds promise as a cathode material for magnesium batteries.

Among tunnel-type  $\text{MnO}_2$  polymorphs, Hollandite ( $\alpha\text{-MnO}_2$ ), characterized by  $2 \times 2$  channels composed of  $\text{MnO}_6$  units, has been extensively studied through density functional theory calculations and charge-discharge characteristics, not only for Li,<sup>[6]</sup> Na,<sup>[7]</sup> and Zn batteries,<sup>[8]</sup> but also for Mg batteries.<sup>[9]</sup> However, Hollandite exhibits low reversibility due to a phase transition from tetragonal to orthorhombic during  $\text{Mg}^{2+}$  insertion; the inserted  $\text{Mg}^{2+}$  is not located at the center of the channel ( $2a/2b$  sites), but at the deviated  $8h$  site, forming a strong Coulomb interaction to cause lattice distortion.<sup>[10]</sup> This loss of reversibility highlights the necessity of selecting tunnel structure materials that do not undergo lattice distortion during Mg insertion.

T. Yabu, R. Iimura, A. Nasu, M. Matsui, H. Kobayashi

Department of Chemistry

Faculty of Science

Hokkaido University

Sapporo 060-0810, Japan

E-mail: h.kobayashi@sci.hokudai.ac.jp

R. Iimura

Institute of Multidisciplinary Research for Advanced Materials

Tohoku University

Sendai 980-8577, Japan

T. Mandai

Research Center for Energy and Environmental Materials

National Institute for Materials Science (NIMS)

Tsukuba 305-0044, Japan



Supporting information for this article is available on the WWW under <https://doi.org/10.1002/batt.202500118>

In this study, we focus on Romanechite, one of the tunnel-type  $\text{MnO}_2$  polymorphs, having an asymmetric  $3 \times 2$  tunnel-type structure. Romanechite has been applied as a cathode material for Li<sup>[11]</sup> and Na batteries,<sup>[11b,12]</sup> exhibiting high-rate performance and robust cycling capability as a host structure. The asymmetric tunnel inherently incorporates  $\text{Ba}^{2+}$  ions, which are expected to act as structural support pillars and alleviate strong Coulombic interactions between  $\text{Mg}^{2+}$  and  $\text{O}^{2-}$ . Additionally, the intrinsic low-symmetry tunnel structure is similar to the distorted structure of  $\text{Mg}^{2+}$  intercalated Hollandite, as mentioned above. This asymmetric tunnel features two  $\text{Mg}^{2+}$  conduction paths, including a 1D path deviated from the center, as shown in Figure S1, Supporting Information. In other words, during discharge,  $\text{Mg}^{2+}$  is likely to occupy the same sites as the  $\text{Ba}^{2+}$  ions. Due to these structural and compositional characteristics, this unique design holds promise for magnesium-ion applications, with its asymmetry expected to mitigate phase transitions during Mg insertion. Here, we succeed in synthesizing Romanechite nanoparticles via an alcohol solution process at room temperature, enabling superior magnesium ion intercalation/extraction compared with Hollandite nanoparticles.

## 2. Results and Discussion

### 2.1. Structure and Morphology

Romanechite nanoparticles were synthesized at a room-temperature alcohol solution process using a redox reaction of  $\text{MnO}_4^-$  and  $\text{Mn}^{2+}$  with a hydrated  $\text{Ba}^{2+}$  cation as a template. Figure 1a shows X-ray diffraction (XRD) patterns of Romanechite and Hollandite nanoparticles. Note that the synthesis of Hollandite nanoparticles is reported in our previous work in detail,<sup>[13]</sup> and the XRD pattern matches  $(\text{NH}_4)\text{Mn}_8\text{O}_{16}$  (PDF No. 01-082-1450). The synthesized Romanechite was identified as  $\text{Ba}_{0.66}\text{Mn}_5\text{O}_{10}(\text{H}_2\text{O})_{1.18}$  (PDF No. 01-084-1683). These XRD patterns were fitted using the Rietveld refinement method (Table S1, Supporting Information). Romanechite with a different crystallite size was also synthesized using the conventional hydrothermal method for comparison, as shown in Figure S2, Supporting

Information.<sup>[14]</sup> Although the hydrothermal product contains some impurities, the similarity of the XRD patterns supports the successful synthesis of Romanechite by the alcohol solution process. The elemental ratio of Ba/Mn (mol/mol) is 0.05, calculated from both the inductively coupled plasma atomic emission spectroscopy (ICP-AES) and scanning electron microscopy (SEM)/energy dispersive X-ray spectrometry (EDX) (shown in Figure S3, Supporting Information) analyses. Notably, Na was hardly detected from the SEM/EDX, suggesting the absence of the precursor  $\text{NaMnO}_4$  or birnessite-type  $\text{MnO}_2$ . The broad XRD peaks suggest the low crystallinity of particles, since the reaction proceeds at room temperature within 60 min, in a 2-propanol solution, in which crystal growth hardly proceeds via the dissolution/recrystallization process compared with hydrothermal conditions.<sup>[11a]</sup> The low Ba content is probably due to the small particle size (i.e., the edge-rich structure) and suggests the capability of a large amount of Mg insertion into the tunnel.

Figure 1b displays the Mn K-edge X-ray absorption near-edge structure (XANES) spectra. The edge position and the white line of Romanechite are almost the same as those of Hollandite, indicating the similarity of the Mn valence state. Since the edge position is between  $\text{Mn}_2\text{O}_3$  and  $\text{MnO}_2$ , the Mn valence state is between trivalent and tetravalent. This finding elucidates the capability of Romanechite to accommodate guest cations within its tunnel structure. Note that the white line peak intensity of Romanechite is weak compared with Hollandite, suggesting lower crystallinity.

Figure 2 shows transmission electron microscopy (TEM) images of Hollandite and Romanechite nanoparticles. SEM images are displayed in Figure S4, Supporting Information. The observed  $d$  value is 0.534 nm, corresponding to the (201) plane of Romanechite (Figure 2d). Usually, tunnel-type oxides have needle-like morphology, as shown in Hollandite (Figure 2a,b), due to the preferred crystal growth along the  $c$ -axis. The particle morphology of the obtained Romanechite (Figure 2c,d) is different from Hollandite or reported crystalline Romanechite,<sup>[11a]</sup> a plate-like morphology, suggesting that the crystal growth proceeds along with not the  $c$ -axis but the  $ab$ -plane. This difference in particle morphology should affect  $\text{Mg}^{2+}$  diffusion.

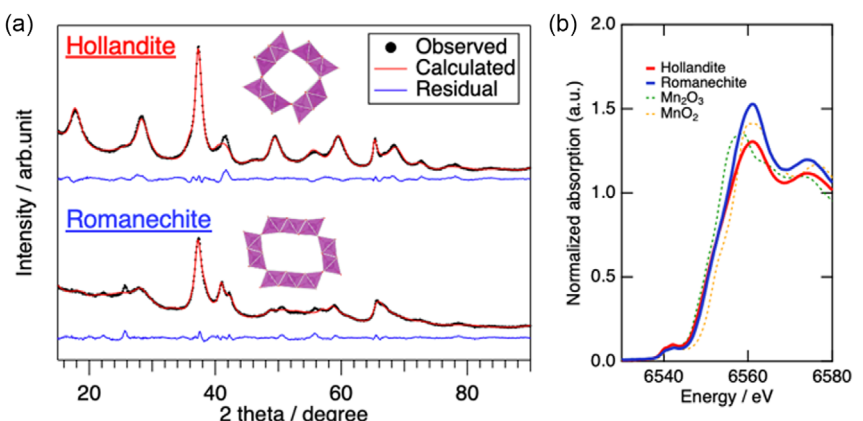


**Figure 1.** a) XRD patterns with fitting curves and b) Mn K-edge XANES spectra of Romanechite, and Hollandite nanoparticles.

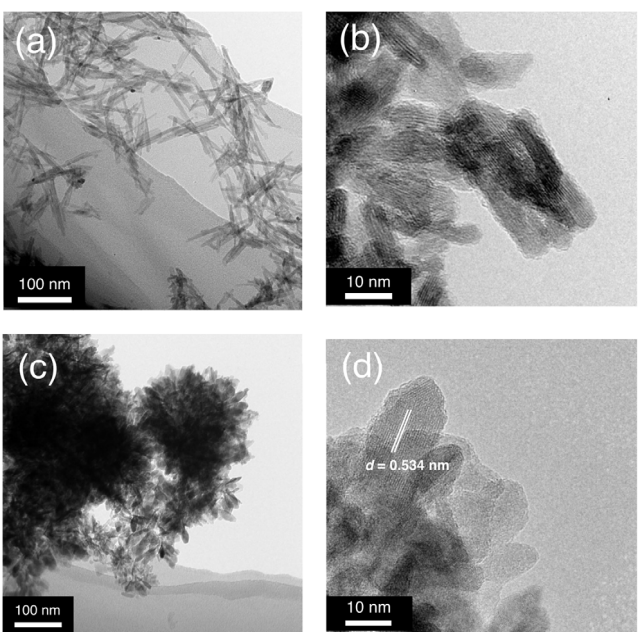


Figure 2. TEM images of a,b) Hollandite c,d) Romanechite nanoparticles.

The  $Mg^{2+}$  diffusion path is located in the tunnel, as shown in Figure S1, Supporting Information, and the diffusion length in solids is quite slow. The plate-like particle has a shortened length along the *c*-axis, enabling rapid  $Mg^{2+}$  insertion/

extraction. A Brunauer–Emmett–Teller (BET) specific surface area of Romanechite is  $72\text{ m}^2\text{ g}^{-1}$ , suggesting the nanoparticle.

## 2.2. Electrochemical $Mg^{2+}$ Intercalation and Extraction

Figure 3a shows the first discharge–charge curves of the Hollandite and Romanechite cathodes. Voltage drops were observed at the beginning of the discharge, attributed to an overvoltage arising from the magnesium metal anode. The discharge capacities were  $231\text{ mAh g}^{-1}$  for Hollandite and  $130\text{ mAh g}^{-1}$  for Romanechite. The lower discharge capacity of Romanechite compared to Hollandite probably stems from the presence of template  $Ba^{2+}$  cations inside the tunnel that can inhibit  $Mg^{2+}$  insertion. On the other hand, the recharging process proceeded up to the theoretical capacity of  $\approx 300\text{ mAh g}^{-1}$ ; it is noteworthy that electrolyte decomposition should occur as a side reaction.

The electrochemical reaction in the RMB involves not only magnesium intercalation/extraction but also side reactions such as electrolyte decomposition catalyzed by  $MnO_2$  and another cation insertion (e.g., traceable proton). Therefore, identifying the amount of Mg in the electrode during the discharge–charge is necessary for clarifying the redox reaction. We measured the Mg/Mn molar ratio from the SEM/EDX analysis, and the quantified value is documented in Figure 3a,c. At the fully discharged state, the rate of Mg intercalation reaction per total electrochemical reaction ( $Mg_D/\eta$ ) is mentioned. Although Hollandite exhibits higher discharge capacity, the discharge reaction involves 28%

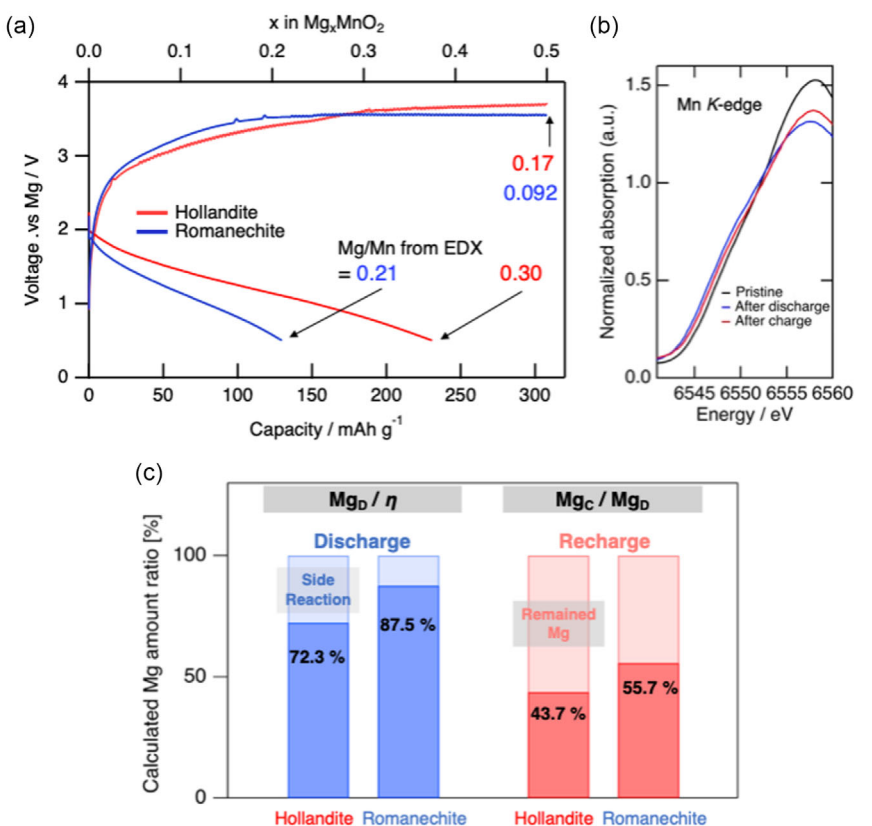


Figure 3. a) Voltage curves of Hollandite and Romanechite cathodes with elemental ratio of Mg/Mn estimated from SEM/EDX, b) magnified Mn *K*-edge XANES of Romanechite, and c) estimated Mg intercalation/extraction contributions during discharge–charge.

side reactions; on the other hand, the side reaction was suppressed to 12% in the Romanechite cathode. At the recharged state, the rate of extracted Mg per intercalated Mg ( $Mg_c/Mg_D$ ) of Romanechite was also higher than Hollandite. These results suggest that Mg intercalation/extraction into Romanechite proceeds with fewer side reactions during discharge–charge, despite its lower crystallinity. On the other hand, given the high specific surface area of Romanechite, it is also possible that capacitive reactions contribute to the observed discharge capacity, occurring in parallel with Mg intercalation. Figure 3b presents the Mn *K*-edge XANES analysis of Romanechite, tracing the redox behavior of Mn during the discharge–charge process. The results indicate a semi-reversible redox process, consistent with the voltage profile shown in Figure 3a. Specifically, the reoxidation of Mn is observed, confirming that the decrease in Mg detected by EDX during the charging process, as shown in Figure 3c.

To support the reversible redox reaction, XRD patterns of the electrodes before and after the discharge–charge are presented in Figure 4. The Hollandite electrode exhibits broad peaks at 26°, 35°, and 41° after discharge; the former single peak is possibly attributed to an asymmetrically distorted tunnel phase in which magnesium was inserted into the 8 *h* site of Hollandite considering the similarity of the XRD pattern with the Romanechite electrode as discussed later, while the latter two peaks are attributable to the rocksalt ( $Mg_xMn_{1-x}O$ ), a fully discharged phase. Additionally, the peak at 29° also disappeared due to the structural distortion induced by magnesium insertion.<sup>[5]</sup> These peaks remain even after the full recharge; only peak shifts of the rocksalt phase to a higher angle were observed. These indicate that the extraction of Mg from the discharged phases hardly occurs. On

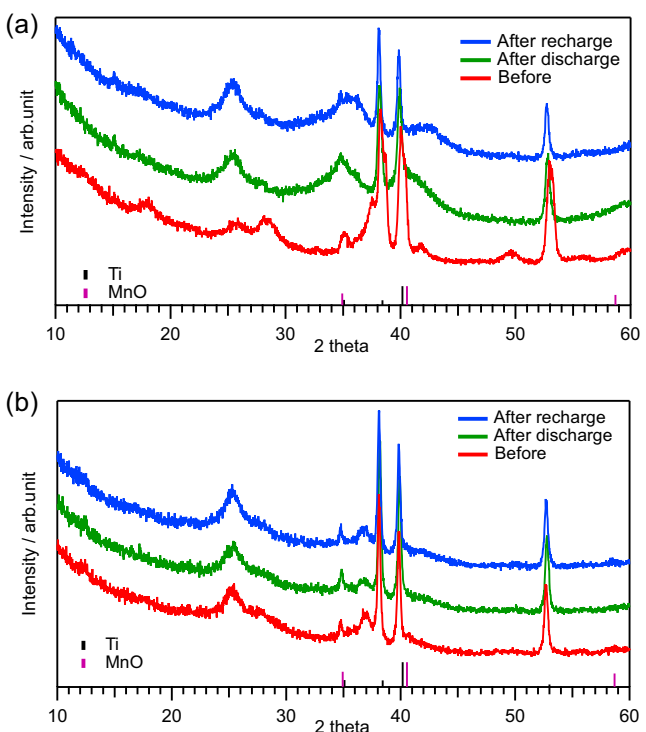


Figure 4. XRD patterns of a) Hollandite and b) Romanechite before and after discharge–charge.

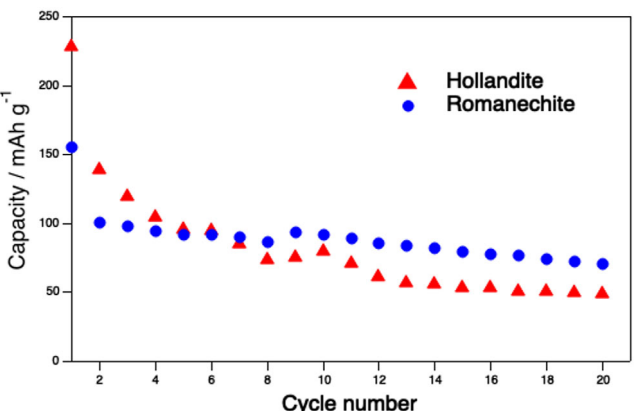


Figure 5. Discharge capacity of Romanechite and Hollandite during 20 cycles at a current density of  $10 \text{ mA g}^{-1}$ .

the other hand, no distinct peak shifts/changes are observed in the Romanechite electrode during the first discharge–charge; no formation of the electrochemically inactive rocksalt phase. The reversible Mg intercalation/extraction is enabled by the stable, distorted tunnel structure.

Although the electrolyte decomposition reaction caused dramatic capacity degradation from the first to the second cycle, Romanechite exhibited superior cycle performance as shown in Figure 5. Capacity retention is 21.3% for Hollandite and 45.7% for Romanechite, demonstrating the latter's superior electrochemical and structural stability during magnesium intercalation and extraction. However, for both Romanechite and Hollandite, significant electrolyte decomposition was observed during the charging process, and in all cycles, the charge capacity reached the cutoff corresponding to the theoretical capacity. The side reactions during the charging process should be mitigated by addressing the interface between the electrolyte and the cathode.

### 3. Conclusion

Nanosized Romanechite, synthesized using an alcohol solution process at room temperature, exhibits a plate-like morphology, having a shortened Mg diffusion length along the *c*-axis. It enables reversible electrochemical Mg intercalation/extraction at room temperature with fewer side reactions compared with Hollandite. The  $MnO_2$  cathode with an asymmetric tunnel structure has an advantage in terms of structural reversibility and is a promising host structure for room-temperature rechargeable magnesium batteries.

### 4. Experimental Section

#### Sample Preparation

Romanechite and Hollandite were prepared via the alcohol solution process. For the synthesis of Romanechite, a solution of  $NaMnO_4 \cdot H_2O$  (3.6 mmol) and  $BaCl_2 \cdot 2H_2O$  (3.9 mmol) in 45 mL of water was added to the  $MnCl_2 \cdot 4H_2O$  (4.5 mmol) solution in 2-propanol (125 mL) under

vigorous stirring, followed by stirring for 1 h at room temperature. The precipitate was filtered, washed with ethanol and water, and dried at 60 °C overnight. For the synthesis of Hollandite,<sup>[13]</sup> a solution of NaMnO<sub>4</sub>·H<sub>2</sub>O (3.1 mmol) and NH<sub>4</sub>Cl (6.4 mmol) in a mixture of 3 mL water and 15 mL acetonitrile was added to the MnCl<sub>2</sub>·4H<sub>2</sub>O (4.5 mmol) solution in 2-propanol (125 mL) under vigorous stirring. The solution was refluxed under vigorous stirring for 1 h, followed by filtration and washing with ethanol and water, then dried at 60 °C overnight. As a trace of previous studies on Romanechite, with minor modifications, Birnessite was synthesized from Mn(NO<sub>3</sub>)<sub>2</sub>, NaOH, and H<sub>2</sub>O<sub>2</sub>, followed by a hydrothermal process to synthesize Romanechite.<sup>[14]</sup>

## Materials Characterization

The XRD patterns were obtained using the Bruker D2 PHASER XE-T Edition. Rietveld refinement was performed using RIETAN-FP.<sup>[15]</sup> The SEM images and EDS were obtained using JSM-IT510A. The TEM images were obtained using the JEM-2100. ICP-AES was using ICPE-9000. The BET specific surface areas using N<sub>2</sub> absorption were measured using BELSORP MAXG. The X-Ray absorption spectroscopy analyzes were conducted at AichiSR. Data were analyzed using Athena.<sup>[16]</sup> TEM and ICP-AES were measured at the Open Facility, Global Facility Center, Creative Research Institution, and Hokkaido University. The conduction pathway was estimated using the bond valence-based energies, with the softBV software,<sup>[17]</sup> and plotted with VESTA.<sup>[18]</sup>

## Electrochemical Tests

Samples were mixed with acetylene black (AB; Denka Black, Denka Co., Ltd.) and polyvinylidene fluoride (PVDF; Kureha Co.) at a respective weight ratio of 60:30:10 in N-methyl-2-pyrrolidone. The obtained slurry was coated on a Ti foil or a carbon-coated Al foil (Nippon Graphite Industries, Ltd.) current collector, followed by cutting into 10 mm diameter disks to make electrodes. The electrodes were dried at 120 °C under vacuum and transferred into an Ar-filled glovebox. The cathode, Mg ribbon anode, and 0.3 M Mg[B(HFIP)<sub>4</sub>]<sub>2</sub>/diglyme (HFIP: hexafluoroisopropyl) electrolyte were assembled in a 2032 coin-type cell with a glass-fiber separator (GF/A). The charge-discharge tests were performed at 10 mA g<sup>-1</sup>, 25 °C in the constant-current mode using TOSCAT-3100.

## Acknowledgements

This work was supported by JSPS KAKENHI (23K13816, 23KJ0214) and JST GteX (JPMJGX23S1).

## Conflict of Interest

The authors declare no conflict of interest.

## Author Contributions

**Takashi Yabu:** formal analysis (lead); investigation (lead); writing—original draft (lead). **Reona Imura:** investigation (supporting); writing—review and editing (supporting). **Akira Nasu:** writing—review and editing (supporting). **Toshihiko Mandai:** resources (lead); writing—review and editing (supporting). **Masaki Matsui:**

supervision (lead); writing—review and editing (supporting). **Hiroaki Kobayashi:** conceptualization (lead); funding acquisition (lead); methodology (lead); project administration (lead); writing—review and editing (lead).

## Data Availability Statement

The data that support the findings of this study are available from the corresponding author upon reasonable request.

**Keywords:** alcohol solution process • cathode materials • magnesium batteries • nanoparticles

- [1] a) J. Muldoon, C. B. Bucur, T. Gregory, *Angew. Chem. Int. Ed.* **2017**, *56*, 12064; b) C. B. Bucur, T. Gregory, A. G. Oliver, J. Muldoon, *J. Phys. Chem. Lett.* **2015**, *6*, 3578; c) H. D. Yoo, I. Shterenberg, Y. Gofer, G. Gershinsky, N. Pour, D. Aurbach, *Energy Environ. Sci.* **2013**, *6*, 2265.
- [2] a) M. M. Huie, D. C. Bock, E. S. Takeuchi, A. C. Marschilok, K. J. Takeuchi, *Coord. Chem. Rev.* **2015**, *287*, 15; b) M. Mao, T. Gao, S. Hou, C. Wang, *Chem. Soc. Rev.* **2018**, *47*, 8804; c) I. D. Johnson, B. J. Ingram, J. Cabana, *ACS Energy Lett.* **2021**, *6*, 1892.
- [3] D. Aurbach, Z. Lu, A. Schechter, Y. Gofer, H. Gizbar, R. Turgeman, Y. Cohen, M. Moshkovich, E. Levi, *Nature* **2000**, *407*, 724.
- [4] a) H. Kobayashi, Y. Fukumi, H. Watanabe, R. Iimura, N. Nishimura, T. Mandai, Y. Tominaga, M. Nakayama, T. Ichitsubo, I. Honma, H. Imai, *ACS Nano* **2023**, *17*, 3135; b) H. Kobayashi, K. Yamaguchi, I. Honma, *RSC Adv.* **2019**, *9*, 36434.
- [5] a) T. Hatakeyama, H. Li, N. L. Okamoto, K. Shimokawa, T. Kawaguchi, H. Tanimura, S. Imashuku, M. Fichtner, T. Ichitsubo, *Chem. Mater.* **2021**, *33*, 6983; b) X. Ye, H. Li, T. Hatakeyama, H. Kobayashi, T. Mandai, N. L. Okamoto, T. Ichitsubo, *ACS Appl. Mater. Interfaces* **2022**, *14*, 56685.
- [6] J. Dai, S. F. Y. Li, K. S. Siow, Z. Gao, *Electrochim. Acta* **2000**, *45*, 2211.
- [7] J. Huang, A. S. Poyraz, S.-Y. Lee, L. Wu, Y. Zhu, A. C. Marschilok, K. J. Takeuchi, E. S. Takeuchi, *ACS Appl. Mater. Interfaces* **2017**, *9*, 4333.
- [8] a) W. Sun, F. Wang, S. Hou, C. Yang, X. Fan, Z. Ma, T. Gao, F. Han, R. Hu, M. Zhu, C. Wang, *J. Am. Chem. Soc.* **2017**, *139*, 9775; b) Y. Yuan, R. Sharpe, K. He, C. Li, M. T. Saray, T. Liu, W. Yao, M. Cheng, H. Jin, S. Wang, K. Amine, R. Shahbazian-Yassar, M. S. Islam, J. Lu, *Nat. Sustainability* **2022**, *5*, 890.
- [9] a) R. Zhang, X. Yu, K.-W. Nam, C. Ling, T. S. Arthur, W. Song, A. M. Knapp, S. N. Ehrlich, X.-Q. Yang, M. Matsui, *Electrochim. Commun.* **2012**, *23*, 110; b) T. S. Arthur, R. Zhang, C. Ling, P.-A. Glans, X. Fan, J. Guo, F. Mizuno, *ACS Appl. Mater. Interfaces* **2014**, *6*, 7004.
- [10] C. Ling, R. Zhang, T. S. Arthur, F. Mizuno, *Chem. Mater.* **2015**, *27*, 5799.
- [11] a) M. Tsuda, H. Arai, Y. Nemoto, Y. Sakurai, *J. Power Sources* **2001**, *102*, 135; b) M. Tsuda, H. Arai, Y. Nemoto, Y. Sakurai, *J. Electrochim. Soc.* **2003**, *150*, A659.
- [12] F. Hu, M. M. Doeff, *J. Power Sources* **2004**, *129*, 296.
- [13] R. Iimura, S. Kawasaki, T. Yabu, S. Tachibana, K. Yamaguchi, T. Mandai, K. Kisu, N. Kitamura, Z. Zhao-Karger, S.-I. Orimo, Y. Idemoto, M. Matsui, M. Fichtner, I. Honma, T. Ichitsubo, H. Kobayashi, *Small* **2025**, *21*, 2411493.
- [14] Q. Feng, K. Yanagisawa, N. Yamasaki, *J. Porous Mater.* **1998**, *5*, 153.
- [15] F. Izumi, K. Momma, *Solid State Phenom.* **2007**, *130*, 15.
- [16] B. Ravel, M. Newville, *J. Synchrotron Rad.* **2005**, *12*, 537.
- [17] a) H. M. Chen, S. Adams, *IUCrJ* **2017**, *4*, 614; b) H. M. Chen, L. L. Wong, S. Adams, *Acta Crystallogr. Sect. B: Struct. Sci., Cryst. Eng. Mater.* **2019**, *75*, 18; c) L. L. Wong, K. C. Phuah, R. Y. Dai, H. M. Chen, W. S. Chew, S. Adams, *Chem. Mater.* **2021**, *33*, 625.
- [18] K. Momma, F. Izumi, *J. Appl. Cryst.* **2008**, *41*, 653.

Manuscript received: February 18, 2025  
 Revised manuscript received: March 26, 2025  
 Version of record online: April 8, 2025